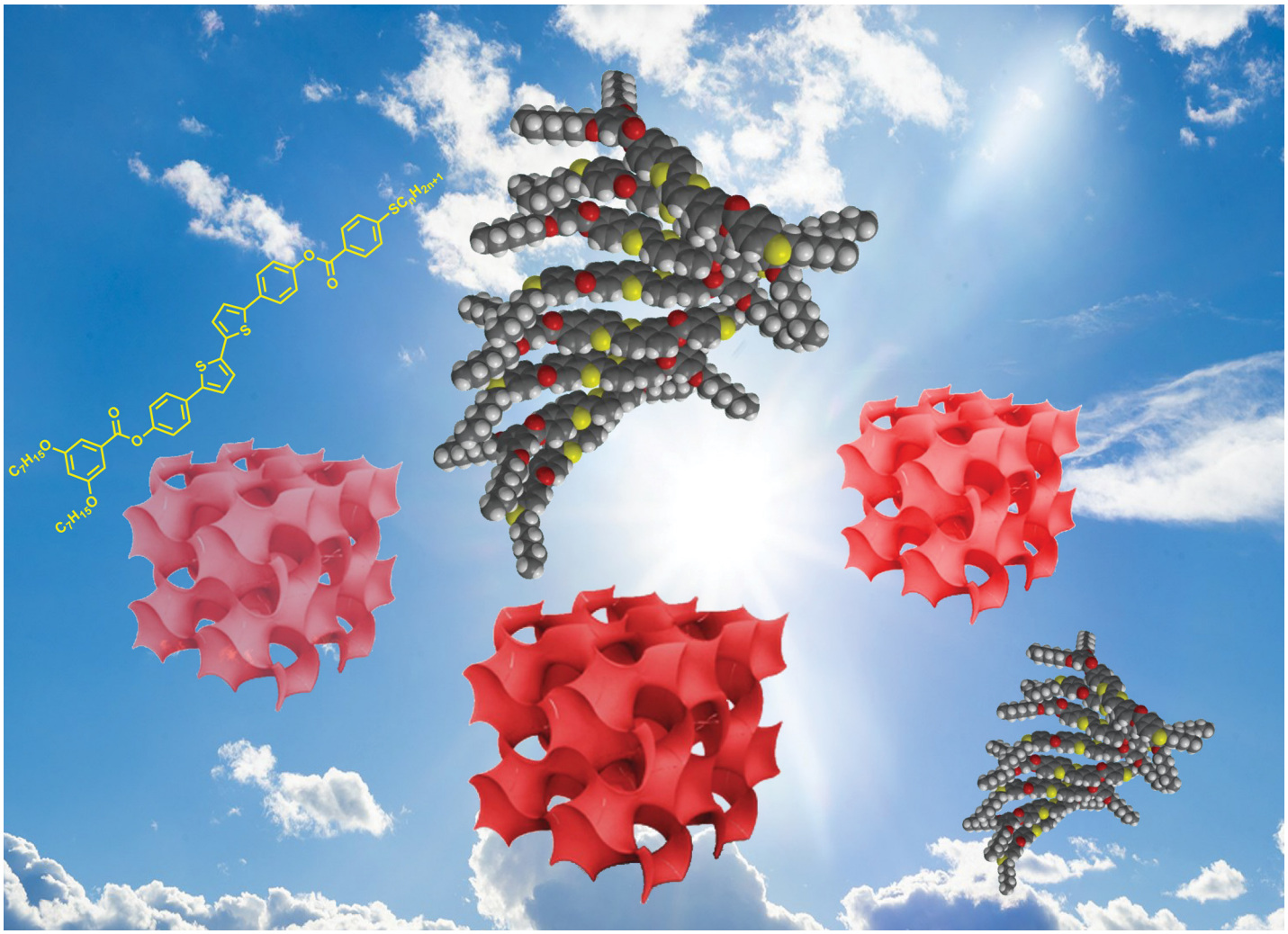

Showcasing research from Professor Alaasar's laboratory, Institute of Chemistry, Faculty of Natural Science II, Martin-Luther-University, Halle-Wittenberg, Germany.

Luminescent and photoconductive liquid crystalline lamellar and helical network phases of achiral polycatenars

New functional achiral bithiophene-based triple chain π-conjugated liquid crystals were synthesized and investigated. They exhibit photoconductivity, photoluminescence (PL), phosphorescence and electroluminescence in both smectic and cubic phases at temperatures up to 150 °C. The smectic phases could be polarized by an applied electric field, which turned a photoresistive device into both a photodiode and a light-emitting diode. Therefore, these materials could be applied in optoelectronic devices. A prototype of such a device, namely a wavelength-measuring photodetector, is demonstrated.

As featured in:

See Mohamed Alaasar, Masafumi Yoshio *et al.*, *Mater. Adv.*, 2024, **5**, 561.

ROYAL SOCIETY OF CHEMISTRY

rsc.li/materials-advances

Registered charity number: 207890

Materials Advances

ROYAL SOCIETY OF CHEMISTRY

PAPER

View Article Online
View Journal | View Issue

Cite this: *Mater. Adv.*, 2024, 5, 561

Luminescent and photoconductive liquid crystalline lamellar and helical network phases of achiral polycatenars†

Mohamed Alaasar, *[ab] Ahmed F. Darweesh,[b] Christian Anders,[a] Konstantin Iakoubovskii[c] and Masafumi Yoshio *[cd]

Received 11th October 2023,
Accepted 12th November 2023

DOI: 10.1039/d3ma00841j

rsc.li/materials-advances

π-Conjugated molecules are of special interest for designing new materials with potential optoelectronic applications. Herein, we report the synthesis of new functional non-symmetric substituted triple-chain π-conjugated 5,5′-diphenyl-2,2′-bithiophenes. They have a long rod-like aromatic core unit with a 3,5-diheptyloxy substituted-pattern at one end and a single thioalkyl or alkoxy chain with variable length at the other end. Their molecular self-assembly was studied by polarized optical microscopy, differential scanning calorimetry, X-ray diffraction, luminescence and photoconductivity techniques. The shortest homologue forms an isotropic liquid phase with a broken mirror symmetry ($Iso_1^{[*]}$) beside smectic and 3D phases. Longer derivatives have no $Iso_1^{[*]}$ or smectic components, and only exhibit 3D phases. The 3D phases are achiral double-gyroid bicontinuous cubic liquid-crystalline (LC) phases with a double helical network structure and $Ia\bar{3}d$ symmetry. Both the smectic and cubic phases exhibit photoconductivity, photoluminescence (PL), phosphorescence and electroluminescence at temperatures up to 150 °C. The smectic liquid crystals show weaker PL, but stronger photoconductivity; they could be polarized by an applied electric field, which turned a photoresistive device into both a photodiode and a light-emitting diode. Hence this work provides new functional bithiophene-based materials, which could be applied in optoelectronic devices. A prototype of such a device, namely a wavelength-measuring photodetector, is demonstrated.

1. Introduction

The design of liquid crystalline (LC) materials with application-relevant nanoscale morphologies provides an important way to functional materials. For example, π-conjugated LC materials[1–3] have several potential applications such as light-emitting diodes,[4,5] photodetectors,[6–8] thin-film transistors,[9–11] photovoltaic cells[12,13] and targeted drug delivery.[4,14,15] In the last decade, a special interest arose in bicontinuous cubic (Cub_{bi}) LC phases. They represent nanosegregated network structures, which can form continuous conduction channels in three dimensions, thus minimizing distortions induced by structural defects, as for example in the case of ion-carrying ionic amphiphiles.[2] A design concept for producing such nanostructured Cub_{bi} phases has been well established during the recent years, based on rod-like molecules terminated by more than two alkyl chains, the so-called polycatenar molecules.[16] Cub_{bi} phases are characterized by their optically isotropic appearance when viewed between crossed polarizers, and were reported for non-symmetric tri- or tetra-catenar molecules having an extended aromatic rod-like core with the terminal chains distributed in a [2+1] or [3+1] fashion, respectively ([3+1] meaning 3 chains on one end and one chain on the other end of the molecule). They were found in π-conjugated 5,5'-diphenyl-2,2′-bithiophene derived materials[16–19] or in molecules incorporating the photoswitchable azobenzene unit.[20–26] In the Cub_{bi} phases, the π-conjugated rods lie almost perpendicularly to the local network direction, with the flexible chains filling the space between the networks. The rod-like units within this arrangement cannot be perfectly parallel, because of the bulky ends formed by the multiple alkyl chains, and therefore a twist is induced (Fig. 1d). The twist is synchronized along the network, adjusting to its structure[27] and resulting in the formation of a helical configuration with uniform chirality along the individual nets. There are two types of these Cub_{bi} phases: one is a double gyroid with space group $Ia\bar{3}d$ ($Cub_{bi}/Ia\bar{3}d$), which is composed of two interwoven networks with three-way

[a] Institute of Chemistry, Martin Luther University Halle-Wittenberg, 06120 Halle, Germany. E-mail: mohamed.alaasar@chemie.uni-halle.de, malaasar@sci.cu.edu.eg
[b] Department of Chemistry, Faculty of Science, Cairo University, 12613 Giza, Egypt
[c] Research Center for Macromolecules & Biomaterials, National Institute for Materials Science, 1-2-1 Sengen, Tsukuba, Ibaraki 305-0047, Japan
[d] Japan Science and Technology Agency, PRESTO, 4-1-8 Honcho, Kawaguchi, Saitama, 332-0012, Japan

† Electronic supplementary information (ESI) available. See DOI: https://doi.org/10.1039/d3ma00841j

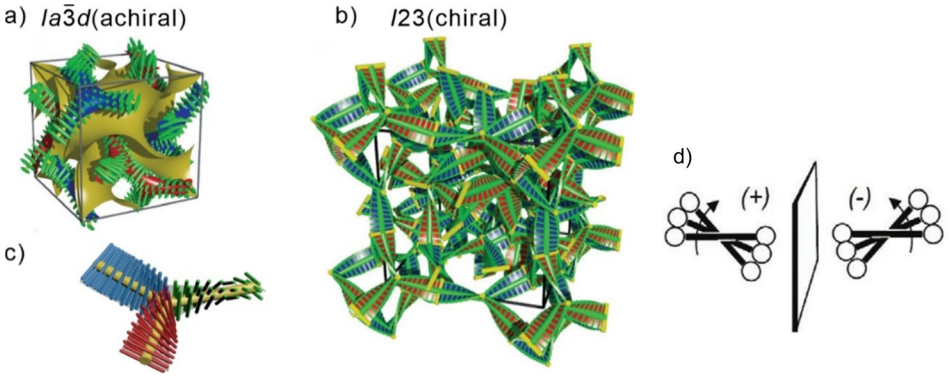

Fig. 1 Helical network structures of the Cub_{bi} phases (a) the achiral double-gyroid $Cub_{bi}/Ia\bar{3}d$ phase and (b) the chiral $Cub_{bi}/I23^{[*]}$ phase; (c) a schematic of a three-way junction interconnecting three network segments formed by the helical stacking of three molecules in the $Cub_{bi}/Ia\bar{3}d$ and $Cub_{bi}/I23^{[*]}$ phases; (d) development of the helical twist by the clashing of the crowded ends attached to the rod-like aromatic cores in the networks, reproduced from ref. 25 by permission from Wiley.

junctions (Fig. 1a–c);[28–31] the other is a triple network structure with the space group $I23$ ($Cub_{bi}/I23^{[*]}$) (Fig. 1b).[32] In the $Cub_{bi}/Ia\bar{3}d$ phase, the two interwoven networks have opposite chiralities, and thus the overall structure is achiral.[33,34] In contrast, for the $Cub_{bi}/I23$ phase, the network chirality cannot be cancelled out, and conglomerates of chiral domains are observed; therefore, this phase is marked with an asterisk, $^{[*]}$. Note that chiral domains were also detected in isotropic liquid phases ($Iso_1^{[*]}$) originating from non-symmetric polycatenars.

Sulfur-containing LC materials[35–40] exhibit strong birefringence owing to the high polarizability of the sulfur atom[41–43] and are of special interest for various applications including liquid crystal displays,[44,45] LC lenses,[46,47] lasers[48] and fast third-order nonlinear switching.[49]

Recently we have reported the synthesis of non-symmetric [3+1] tetracatenars based on the π-conjugated rod-like 5,5′-diphenyl-2,2′-dithiophene unit terminated with three alkoxy and one thioalkyl chains (compounds **A*m*/*n***, Scheme 1). We have characterized the structure and LC phases in those polycatenars, but did not investigate their optoelectronic properties and possible applications.[19]

Herein we report the synthesis and characterization of two new series of related [2+1] tricatenar liquid crystals (compounds **S*n*** and **O*n***, Scheme 1 and Scheme S1 in the ESI†). We discuss the effects of the length and structure of the alkyl chains on the LC properties, and, importantly, demonstrate potential applications of these materials in optoelectronic devices.

2. Experimental details

2.1. Synthesis

The synthesis details and related analytical data are provided in the ESI.†

2.2. Characterization methods

Polarized optical micrographs (POMs) were acquired under the crossed Nicol's condition. Differential scanning calorimetry (DSC) traces were measured with DSC-7 and DSC-8000 Perkin-Elmer setups, in Ar flow, at a heating or cooling rate of 10 K min^{-1}. X-Ray diffraction (XRD) patterns were recorded using $Cu_{K\alpha}$ radiation in the small-angle X-ray scattering (SAXS) and wide-angle X-ray scattering (WAXS) configurations.

Luminescence spectra were acquired with an FP-8300 spectrometer (Jasco, Japan) using a built-in Xe lamp filtered by a single-grating monochromator (intensity at the sample ~10 mW cm^{-2}) for excitation. The same spectrometer was used for spectral electroluminescence (EL) and photoconductivity measurements. Calibrated AM1.5 illumination (100 mW cm^{-2}) was provided by a HAL-C100 Solar Simulator (Asahi Spectrum, Japan).

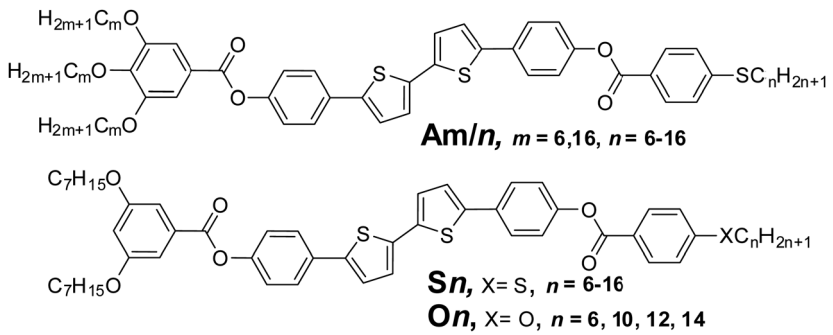

Scheme 1 Molecular structures of the previously reported tetracatenars **A*m*/*n***[19] (top) and the newly synthesized tricatenars **S*n*** and **O*n*** series (below).

Low-fluorescence silica was used as a sample support for luminescence measurements.

Doping with [6,6]-phenyl C_{61} butyric acid methyl ester (PCBM) was performed as follows: 5 mg of sample and 0.5 mg of PCBM were dissolved in 1 mL of chloroform, which was then evaporated at 60 °C.

Optoelectronic devices were prepared by filling commercial cells from EHC, Japan. The cells consisted of two glass plates coated with 20 nm of indium tin oxide (ITO). Epoxy spacers separated them by a distance of 2, 4 or 9 μm. The overlapping area between the top and bottom electrodes was 4 × 4 mm. Cells were filled in a vacuum, in darkness, at a temperature ~5 °C above the isotropic temperature, typically within 1 hour. A small amount of powdered material was placed on the edge of a cell, where it melted, and was driven into the cell by the capillary force.

3. Results and discussion

Fig. 2 shows the mesophase types and phase transition temperatures of the series ***Sn*** measured by DSC upon cooling.

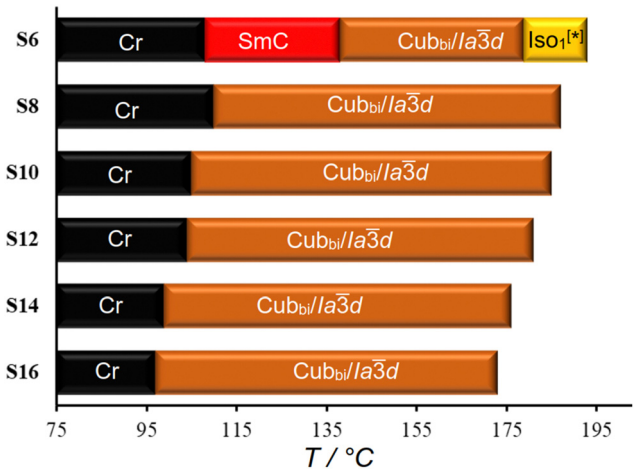

Fig. 2 Phase transitions of compounds ***Sn*** as observed on 2nd cooling with a rate of 10 K min^{-1}.

The numerical data with associated enthalpy values recorded on heating and cooling are summarized in Table 1. Example DSC thermograms of **S6** and **S16** are given in Fig. 3, while those of other compounds can be found in the ESI.†

In the next section the molecular self-assembly of compounds ***Sn*** will be discussed, followed by a comparison with related ***On*** analogues (Section 3.3). Then we present their optoelectronic properties.

3.1. Liquid crystalline behavior

As can be seen from Table 1 and Fig. 2–4 a single Cub$_{bi}$/$Ia\bar{3}d$ LC phase is observed in a wide temperature range for all the reported tricatenars, except for **S6**, which has an additional smectic phase (Fig. 4d and **S29**). Its birefringent schlieren texture did not convert to a dark one under applied shear, as typically observed in the case of the uniaxial SmA phase. Hence, we assign this texture to the SmC phase, and this assignment agrees with XRD results.

XRD pattern of the birefringent **S6** phase shows a single sharp peak at ~1.8° (4.8 nm) and a broad halo at ~20° (0.4 nm, Fig. 5a). Upon heating above 142 °C, the halo is preserved, but the low-angle peak shifts and splits into a doublet, which can be indexed to the (211) and (220) reflections of an $Ia\bar{3}d$ phase with a lattice parameter a_{cub} = 9.9 nm (Fig. 5b). This phase is consistent with the absence of chiral domains in the corresponding optical image (Fig. 4c).

The Cub$_{bi}$/$Ia\bar{3}d$ phase is the only LC phase exhibited by the **S8–S16** homologues, as revealed by the optical textures and the XRD patterns (see Fig. S27 for XRD, ESI†). Its lattice parameter a_{cub} = 9.9–10.6 nm (Table 1) is close to those of the previously reported Cub$_{bi}$/$Ia\bar{3}d$ phases.[17–19] For all members, there is a 6–17 K supercooling of the Iso–Cub$_{bi}$/$Ia\bar{3}d$ transition compared to the Cub$_{bi}$/$Ia\bar{3}d$–Iso transition temperature on heating, which is a common feature for 3D cubic LC phases (Table 1).[50]

3.2. Mirror symmetry breaking in an isotropic liquid network phase

As can be seen from Fig. 3a and Table 1 a transition between two different types of liquid phases is observed in **S6** upon cooling.

Table 1 Phase transitions of compounds ***Sn***[a]

Comp.	Phase transitions T/°C [ΔH/kJ mol^{-1}]	a_{cub}/nm (T/°C)
S6	H: Cr 133 [23.0] SmC 142 [0.5] Cub$_{bi}$/$Ia\bar{3}d$ 196 [1.5] Iso	9.9
	C: Iso 193 [−0.7] Iso$_1^{[*]}$ 179 [−1.4] Cub$_{bi}$/$Ia\bar{3}d$ 138 [<0.1] SmC 108 [−21.7] Cr	(140)
S8	H: Cr 128 [34.8] Cub$_{bi}$/$Ia\bar{3}d$ 196 [2.6] Iso	10.0
	C: Iso 187 [−1.9] Cub$_{bi}$/$Ia\bar{3}d$ 110 [−23.9] Cr	(140)
S10	H: Cr 130 [19.3] Cub$_{bi}$/$Ia\bar{3}d$ 193 [1.7] Iso	10.1
	C: Iso 185 [−1.4] Cub$_{bi}$/$Ia\bar{3}d$ 105 [−18.1] Cr	(140)
S12	H: Cr 122 [28.8] Cub$_{bi}$/$Ia\bar{3}d$ 188 [2.7] Iso	10.3
	C: Iso 181 [−2.1] Cub$_{bi}$/$Ia\bar{3}d$ 104 [−27.3] Cr	(140)
S14	H: Cr 113 [29.3] Cub$_{bi}$/$Ia\bar{3}d$ 183 [1.5] Iso	10.4
	C: Iso 176 [−1.3] Cub$_{bi}$/$Ia\bar{3}d$ 99 [−30.0] Cr	(130)
S16	H: Cr 110 [50.5] Cub$_{bi}$/$Ia\bar{3}d$ 179 [2.4] Iso	10.6
	C: Iso 173 [−2.2] Cub$_{bi}$/$Ia\bar{3}d$ 97 [−45.2] Cr	(130)

[a] Peak temperatures as determined by DSC upon 2nd heating (H:) and 2nd cooling (C:) with a rate of 10 K min^{-1}. Abbreviations: Cr = crystalline solid phase; Iso = isotropic liquid phase; Iso$_1^{[*]}$ = isotropic liquid phase with spontaneously broken symmetry; SmC = smectic C phase; Cub$_{bi}$/$Ia\bar{3}d$ = achiral bicontinuous cubic phase with $Ia\bar{3}d$ space group; a_{cub} = lattice parameter of the cubic phase.

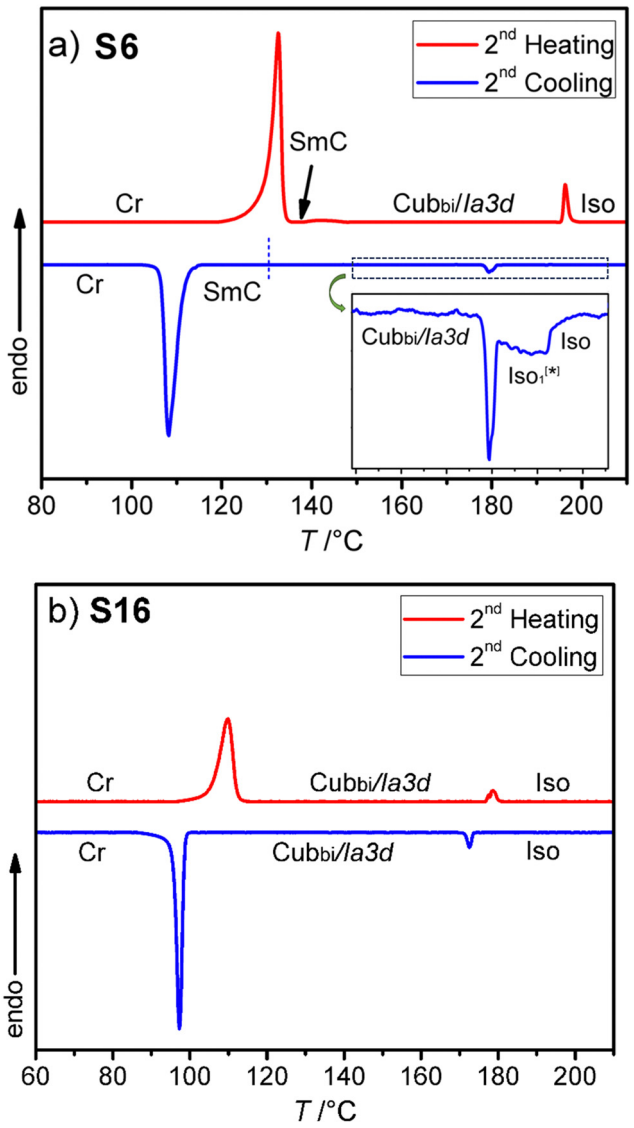

Fig. 3 DSC heating and cooling traces for compounds: (a) **S6** and (b) **S16**. The inset in (a) shows an enlarged view of the Iso-$Iso_1^{[*]}$-$Cub_{bi}/Ia\bar{3}d$ transition on cooling.

This peak is broad; it is associated with a small value of enthalpy change ~0.7 kJ mol^{-1} and is followed by a sharp transition to the cubic phase. At the onset of this broad transition, dark and bright domains could be observed under crossed, and slightly misaligned polarizers. Their contrast can be inverted by reversing the rotation direction of the analyzer (Fig. 4a and b), indicating the presence of chiral domains in this liquid phase. This isotropic liquid phase with a broken mirror symmetry is labeled as $Iso_1^{[*]}$, and is considered as percolated liquid with a dynamic helical network structure similar to those reported for other related non-symmetric polycatenars.[16–19,23] This phase was only observed for the short-chain compound **S6**.

3.3. Replacing the thioalkyl chain with an alkoxy chain

As represented graphically in Fig. 6 and numerically in Table 2, the effect of replacing the thioalkyl chain with an alkoxy chain

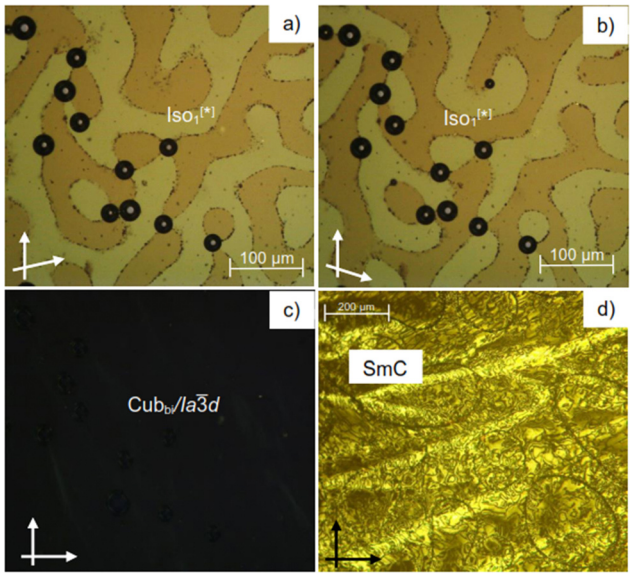

Fig. 4 Cross-polarized optical micrographs of compound **S6** on cooling: (a) and (b) the chiral $Iso_1^{[*]}$ phase at 190 °C for intentionally misaligned polarizers (see white arrows); (c) non-birefringent texture of the achiral $Cub_{bi}/Ia\bar{3}d$ phase at 160 °C and (d) schlieren texture in the SmC texture at 130 °C.

was tested by synthesizing the new compounds ***On***. In contrast to the compound **S6**, the $Cub_{bi}/Ia\bar{3}d$ phase is absent for the shortest derivative **O6**, and only the SmC phase is observed up to the isotropic point (Fig. 6 and **S28**). The SmC phase in both **S6** and **O6** could be aligned by unidirectional flow of the molten compound, as demonstrated in Fig. S29 (ESI†).

Other ***On*** compounds exhibit only the $Cub_{bi}/Ia\bar{3}d$ LC phase, like the ***Sn*** series. However, as can be seen from Tables 1, 2 and Fig. 2, 6, the temperature ranges of the $Cub_{bi}/Ia\bar{3}d$ phase are wider for ***On*** than ***Sn*** polycatenars. This observation can be explained by the more pronounced bending angle resulting from the replacement of the ether linkage (C–O–C, 114°) with the thioether one (C–S–C, 99°),[51] leading to a shift in the molecular shape from nearly rod-like to a more bent configuration. Additionally, this change is accompanied by an increased bond length (C–S, 1.82 nm) compared to C–O (1.45 nm),[51] resulting in a decreased rotational barrier around the C–S bond (S–CH_3: 8.4 kJ mol^{-1}) compared to that of the C–O bond (O–CH_3: 11.3 kJ mol^{-1}).[52,53] These combined effects lead to enhanced conformational chain disorder, reducing the stability of the $Cub_{bi}/Ia\bar{3}d$ phase in the case of thioalkyl-terminated polycatenars (***Sn***) compared to their alkoxy-terminated counterparts (***On***).[54,55]

3.4. Comparison with related tetracatenars

It is important to compare the phase behavior and LC phase types observed in the thioalkyl-chain-terminated tricatenars reported herein (***Sn***) with their related tetracatenars reported before ***Am/n***.[19] As could be seen from Scheme 1, both types of compounds have the same aromatic rod-like backbone and differ only in the number of the terminal alkoxy chain, where two alkoxy chains are used in the new materials (***Sn***), and

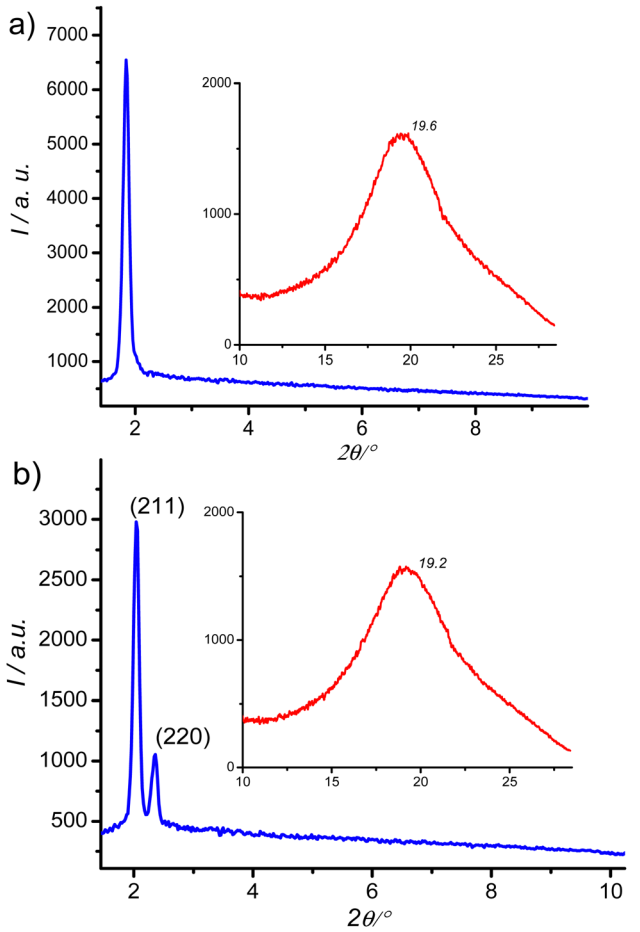

Fig. 5 SAXS patterns of compound **S6** as recorded on cooling: (a) at T = 129 °C in the SmC phase and (b) at T = 160 °C in the Cub$_{bi}$/$Ia\bar{3}d$ phase. The insets show the halo peaks detected in the wide-angle region.

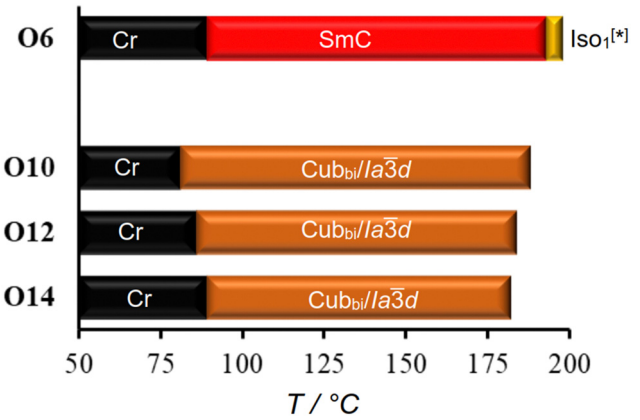

Fig. 6 Phase transitions of compounds **On** as observed on cooling with a rate of 10 K min^{-1}.

an additional third one is introduced in the case of **Am**/***n*** compounds.

Comparing the phase behavior of compounds **A6**/***n*** having three hexyloxy chains to **S*n*** materials having two heptyloxy chains revealed the following: in all cases the melting and crystallization temperatures of **A6**/***n*** derivatives are lower compared to those of **S*n*** homologues because of the enhanced flexibility introduced by the large number of alkoxy chains in **A6**/***n*** compounds. Both shortest homologues from the two series (**A6/6** and **S6**) display Cub$_{bi}$/$Ia\bar{3}d$ and Iso$_1^{[*]}$ phases. However, the SmC phase was only formed by **S6** and not by **A6/6**. This fact could be explained by increased twisting of the whole molecular structure because of the large size of the crowded end in the case of **A6/6**. Such twisting favored the formation of network phases rather than lamellar phases, such as the SmC phase exhibited by **S6**. The lattice parameter of the Cub$_{bi}$/$Ia\bar{3}d$ phases is similar for **S*n*** derivatives (a_{cub} = 9.9–10.6 nm, Table 1) and **A6**/***n*** analogues (~10.6 nm). However, tetracatenars exhibit additional three network phases, such as tetragonal and the triple network chiral Cub$_{bi}$/$I23^{[*]}$ phases, which are not observed in any of **S*n*** derivatives. A further increase in the alkoxy chains length, which was realized in compounds **A10**/***n***, leads to the formation of two different types of achiral double gyroid phases separated by the chiral Cub$_{bi}$/$I23^{[*]}$ phase, and thus an overall phase sequence of Cub$_{bi}$/$Ia\bar{3}d$–Cub$_{bi}$/$I23^{[*]}$–Cub$_{bi}$/$Ia\bar{3}d$,[19] which is not observed in the case of the newly reported tricatenars (**S*n***). This fact can be attributed to the smaller chain volume in **S*n*** compounds as compared to the **A10**/***n*** tetracatenars. Finally, replacing the thioalkyl chain by alkyloxy chain, either in the tricatenars **S*n*** or in the teracatenars **A10**/***n***, does not alter the LC phases, and only slightly shifts the phase transition temperatures, as discussed in Section 3.3 and in our previous report.[19]

Table 2 Phase transitions of compounds **On**[a]

Comp.	Phase transitions T/°C [ΔH/kJ mol^{-1}]
O6	H: Cr 121 [30.7] SmC 197 [1.4] Iso$_1^{[*]}$ 200 [<0.1] Iso C: Iso 198 [<0.1] Iso$_1^{[*]}$ 193 [−1.8] SmC 89 [−25.0] Cr
O10	H: Cr 118 [20.0] Cub$_{bi}$/$Ia\bar{3}d$ 198 [1.8] Iso C: Iso 188 [−1.2] Cub$_{bi}$/$Ia\bar{3}d$ 81 [−19.3] Cr
O12	H: Cr 118 [38.8] Cub$_{bi}$/$Ia\bar{3}d$ 193 [3.1] Iso C: Iso 184 [−2.2] Cub$_{bi}$/$Ia\bar{3}d$ 86 [−49.2] Cr
O14	H: Cr 106 [32.2] Cub$_{bi}$/$Ia\bar{3}d$ 189 [2.6] Iso C: Iso 182 [−2.0] Cub$_{bi}$/$Ia\bar{3}d$ 89 [−28.5] Cr

[a] Peak temperatures as determined by the DSC upon 2nd heating (H:) and 2nd cooling (C:) scans with a rate of 10 K min^{-1}.

The newly reported tricatenars (**S*n*** and **O*n***) complete the reported family of nonsymmetric polycatenar materials. In contrast to the (predominantly cubic) tetracatenars, the tricatenars exhibit linear SmC phases that can be aligned by electric field. This property is essential for the potential photoelectronic devices that are described in the following sections. Meanwhile, as demonstrated in Fig. S31 (ESI†), the cubic phases exhibit stronger luminescence compared to smectic phases, which may be important for optical applications.

3.5. Dark and photoconductivity

Photoconductivity under AM1.5 illumination was observed both for **S*n*** and **O*n*** series. It was *ca.* 10 times stronger in smectic-phase compounds **S6** and **O6** than in longer-chain

materials. Photoconductivity will be demonstrated using **O6** as a representative example.

Filling a symmetrical ITO cell with **O6** created a photoresistor exhibiting quasi-symmetrical *I–V* characteristics and a short-circuit current $I_{SC} \sim 50$ nA cm^{-2} under AM1.5 illumination. This I_{SC} value increased 10 times after poling, a standard procedure in LC transport measurements,[56] which involves heating the material from the crystal into the LC phase to induce reorientation of polar fragments in the constituent molecules. The polar fragments in **O6**, such as carbonyl groups with a dipole moment of ~3 D, as estimated by density functional theory, underwent reorientation in response to electric field (4 V μm^{-1} in this case) applied to the device, and cooling the material down into the crystal phase, locked its molecules in the oriented state. Poling transformed the **O6**-based device from a photoresistor into a photodiode (Fig. 7a). Its photocurrent under AM1.5 illumination was relatively small, presumably due to the weak absorption of visible light by the **O6** compound, as evidenced by the photocurrent spectrum shown by the black curve in Fig. 7b.

To increase absorption of visible light in **O6**, we have doped it with 10 mol% of PCBM. As a result, I_{SC} increased up to 6 μA cm^{-2} without affecting the phase transitions, as confirmed by temperature-resolved optical microscopy. This enhancement can be attributed to the accepting properties of PCBM and strong absorption in the visible range, which was imparted to the doped **O6** sample as seen in Fig. 7b. We have attempted to further increase the I_{SC} through heavier doping, but found, by combined optical and XRD measurements, that PCBM was precipitated at concentrations above 10 mol%.

Devices prepared by flowing **O6** into a 4 μm-thick ITO-ITO cell retained their quasi-symmetrical nature even after poling. In particular, the sign of their photocurrent would change depending on the direction and wavelength of illumination. This phenomenon is known as dual-polarity photocurrent.[57] It can be explained by a simple band diagram outlined in Fig. 8.

We found that for wavelength ranging from 300 to 700 nm the sign of photocurrent can be controlled by applying a small voltage (within ±0.3 V) to the device. Interestingly, the value of this "control voltage" remained almost constant irrespective of the light intensity within the range 1–10 mW cm^{-2}. As a result, we could estimate the illuminating wavelength, with an accuracy of ±5 nm, by comparing the bias voltage resulting in a zero photocurrent with a calibration curve (depicted as a dashed line in Fig. 9). Although the calibration curve is a non-monotonous function that can have equal values for two different wavelengths (*e.g.* 0.15 V for 440 and 670 nm), this ambiguity can be resolved by noting the sign of photocurrent, which is positive for 440 nm and negative at 670 nm at the same 0.15 V bias.

Finding a zero-photocurrent bias was achieved with a simple electronic circuit equipped with a feedback loop. Combining this circuit with a photodetector based on the PCBM-doped compound **O6**, yields a prototype device that can estimate illumination wavelength in the 300–700 nm range without the use of bulky and costly optical dispersive elements.

3.6. Photoluminescence, phosphorescence, and electroluminescence

All studied solid compounds exhibited strong greenish luminescence under UV illumination with a wavelength in the range of 300–460 nm. Their quantum efficiency was estimated using cerium-doped yttrium aluminium garnet.[56] The efficiency varied between 2 and 20% depending on the material and LC phase. For example, in the same sample of compound **S6**, luminescence was weaker in the smectic than in the cubic phase (Fig. S31, ESI†), possibly due to the higher packing density and stronger intermolecular interactions in the smectic phase. Apart from efficiency, we did not observe any significant material dependence for other luminescence properties, such as spectral and temporal dependences of emission and excitation. Thus, we shall illustrate these properties on example of **O6**, as it exhibited the strongest EL among the studied compounds, with an efficiency reaching ~0.1%.

The black line in Fig. 10a shows a characteristic room-temperature luminescence spectrum from undoped **O6** excited at 360 nm. The spectrum consists of two overlapping bands

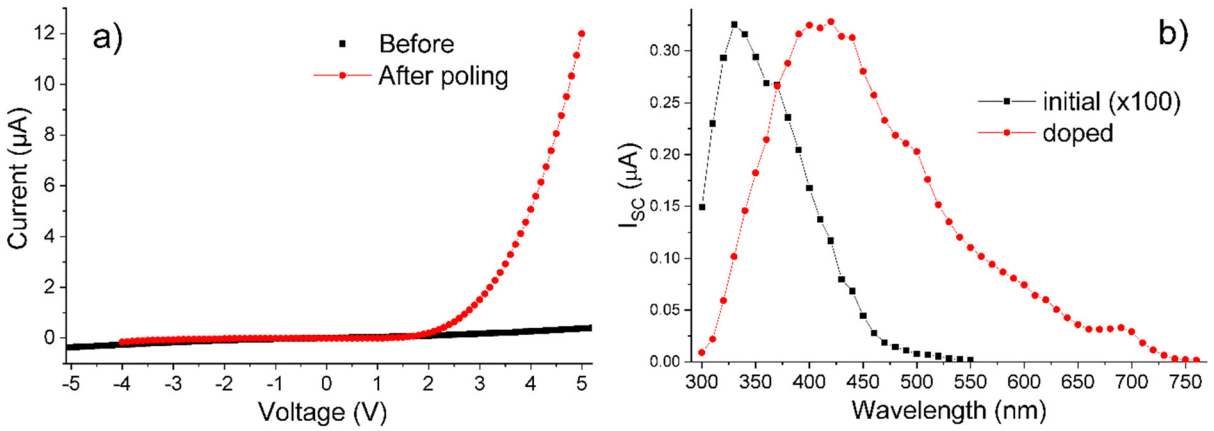

Fig. 7 Optoelectronic properties of **O6** in a 2 μm-thick ITO-ITO cell: (a) dark *I–V* curves before and after poling. (b) Spectra of short-circuit photocurrent, measured after poling, for undoped and 10 mol% PCBM doped material.

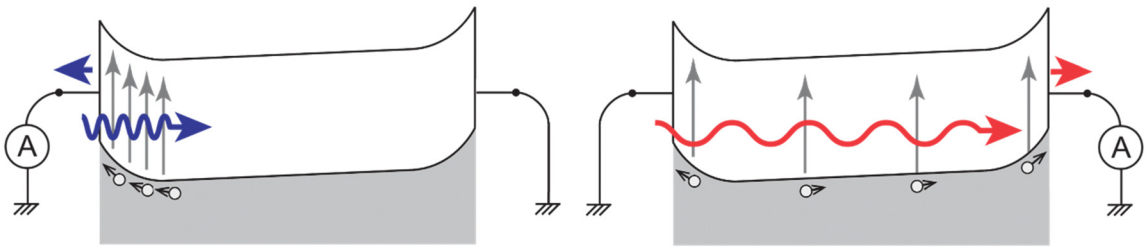

Fig. 8 Schematic of photocurrent processes in a slightly asymmetric device irradiated with strongly absorbed blue light (left) and weakly absorbed red light (right). It reveals that photocurrent can change its direction depending on the wavelength. The asymmetry is induced by internal electric field that was created in the material by poling. Only hole transport is considered, as appropriate for an acceptor-doped material, such as PCBM-doped **O6**.

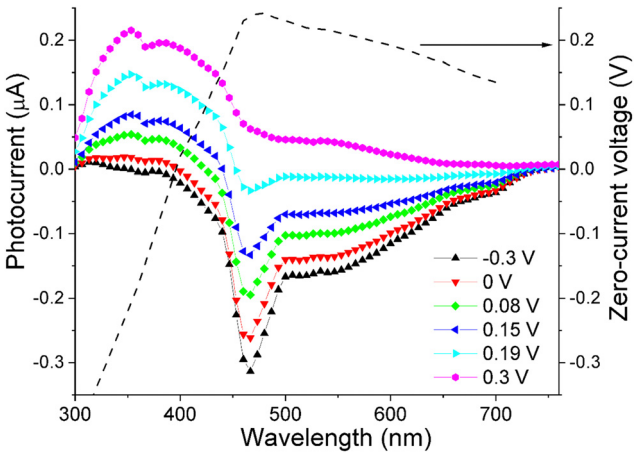

Fig. 9 Photocurrent spectra from PCBM-doped **O6** in a 4 μm-thick cell measured at room temperature and at indicated voltages. The dashed curve shows the value of voltage that results in a zero photocurrent.

centered at *ca.* 490 nm and 550 nm. When the luminescence is measured not simultaneously with optically modulated excitation, but after a 1 ms delay, the 490 nm band significantly weakens as compared to the 550 nm emission, indicating that the latter originates from phosphorescence. When emission is excited, in the same sample, not by UV light, but by electric current, only the 550 nm band is observed, and its time dependence under square-pulse excitation shows a lifetime on the order of 1 ms (Fig. 10b). Doping of **O6** with 10 mol% of PCBM induces a new EL band at 725 nm, which can be assigned to the emission from PCBM molecules (Fig. 10a). Note that while the spectra of Fig. 10 were measured at room temperature, all the reported phenomena persisted up to at least 150 °C. They can be rationalized as follows: the studied ***Sn*** and ***On*** compounds exhibit a photoluminescence band at 490 nm and a phosphorescence band at 550 nm, they also exhibit EL at 550 nm, which results from the phosphorescence band. The EL spectrum can be extended from *ca.* 450–650 nm to 500–850 nm by doping with PCBM.

4. Summary and conclusions

We have reported the synthesis and molecular self-assembly of two new series of π-conjugated non-symmetric substituted triple-chain 5,5′-diphenyl-2,2′-bithiophenes. They have the same extended rod-like aromatic core, terminated by two heptyloxy chains at one end and one thioalkyl (series ***Sn***) or alkoxy chain (series ***On***) with a variable length at the other end.

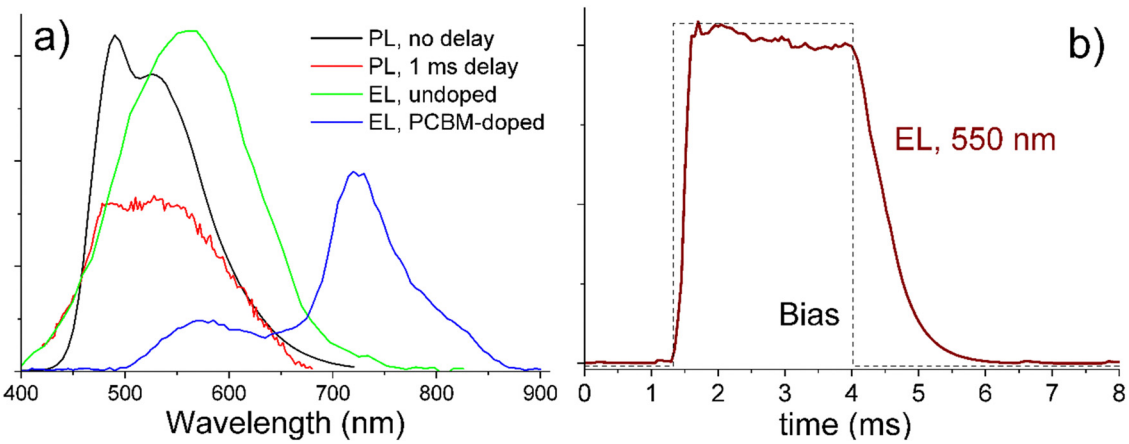

Fig. 10 (a) Room-temperature spectra of electroluminescence, conventional luminescence and luminescence recorded 1 ms after switching off the excitation light (phosphorescence) in compound **O6**. Intensity is arbitrary for all curves. (b) Time behavior of electroluminescence intensity at 550 nm for undoped **O6** excited with a square current pulse.

All materials were investigated for their LC behavior using polarized optical microscopy, differential scanning calorimetry and X-ray diffraction. Additionally, they were also characterized by luminescence and photoconductivity techniques for their possible applications. Three different phases were observed in these polycatenars, including smectic C, helical-network bicontinuous cubic phase with $Ia\bar{3}d$ symmetry ($Cub_{bi}/Ia\bar{3}d$), and an isotropic liquid phase with a broken mirror symmetry ($Iso_1^{[\star]}$). Replacing the sulfur with oxygen in the thioalkyl chain retains the cubic LC phases and widens their temperature ranges. Photoconductivity, phosphorescence, and electroluminescence at temperatures up to 150 °C were found in both smectic and cubic phases. A protype of an optoelectronic device (a wavelength-measuring photodetector) was successfully demonstrated. Therefore, this work provides new functional nanostructured materials, which could be applied in optoelectronic devices.

Conflicts of interest

There are no conflicts to declare.

Acknowledgements

M. Alaasar acknowledges the German Research Foundation (DFG) for the financial support (AL2378/1-2, no. 424355983). A. F. Darweesh acknowledges the support by the Alexander von Humboldt Foundation for the research fellowship at the Martin Luther University Halle-Wittenberg, Germany. M. Yoshio gratefully acknowledges financial support from the Japan Society for the Promotion of Science (no. 21H02021), Japan Science and Technology Agency (no. JPMJPR23QB) and Iketani Science and Technology Foundation (no. 0351202-A).

References

1 W. Pisula, M. Zorn, J. Y. Chang, K. Müllen and R. Zentel, *Macromol. Rapid Commun.*, 2009, **30**, 1179–1202.
2 T. Kato, M. Yoshio, T. Ichikawa, B. Soberats, H. Ohno and M. Funahashi, *Nat. Rev. Mater.*, 2017, **2**, 17001.
3 H. K. Bisoyi and Q. Li, *Prog. Mater. Sci.*, 2019, **104**, 1–52.
4 T. Yasuda, H. Ooi, J. Morita, Y. Akama, K. Minoura, M. Funahashi, T. Shimomura and T. Kato, *Adv. Funct. Mater.*, 2009, **19**, 411–419.
5 C. Keum, D. Becker, E. Archer, H. Bock, H. Kitzerow, M. Gather and C. Murawski, *Adv. Opt. Mater.*, 2020, **8**, 2000414.
6 M. Hecht, T. Schlossarek, M. Stolte, M. Lehmann and F. Würthner, *Angew. Chem., Int. Ed.*, 2019, **58**, 12979–12983.
7 A. Calò, P. Stoliar, M. Cavallini, Y. H. Geets and F. Biscarini, *Org. Electron.*, 2011, **12**, 851–956.
8 M. Dechant, M. Lehmann, G. Uzurano, A. Fujii and M. Ozaki, *J. Mater. Chem. C*, 2021, **9**, 5689–5698.
9 H. Iino, T. Usui and J. Hanna, *Nat. Commun.*, 2015, **6**, 6828.
10 D. H. Kim, B.-L. Lee, H. Moon, H. M. Kang, E. J. Jeong, J.-I. Park, K.-M. Han, S. Lee, B. W. Yoo, B. W. Koo, J. Y. Kim, W. H. Lee, K. Cho, H. A. Becerril and Z. Bao, *J. Am. Chem. Soc.*, 2009, **131**, 6124–6132.
11 O. Kwon, X. Cai, W. Qu, F. Liu, J. Szydlowska, E. Gorecka, M. J. Han, D. K. Yoon, S. Poppe and C. Tschierske, *Adv. Funct. Mater.*, 2021, **31**, 2102271.
12 M. Kumar and S. Kumar, *Polym. J.*, 2017, **49**, 85–111.
13 M. Funahashi, *Mater. Chem. Front.*, 2021, **5**, 8265–8274.
14 E. Bukusoglu, M. B. Pantoja, P. C. Mushenheim, X. Wang and N. L. Abbott, *Annu. Rev. Chem. Biomol. Eng.*, 2016, **7**, 163–196.
15 Y. Chen, P. Ma and S. Gui, *BioMed Res. Int.*, 2014, 1–12.
16 C. Dressel, T. Reppe, S. Poppe, M. Prehm, H. Lu, X. Zeng, G. Ungar and C. Tschierske, *Adv. Funct. Mater.*, 2020, 2004353.
17 T. Reppe, S. Poppe, X. Cai, Y. Cao, F. Liu and C. Tschierske, *Chem. Sci.*, 2020, **11**, 5902–5908.
18 T. Reppe, C. Dressel, S. Poppe, A. Eremin and C. Tschierske, *Adv. Opt. Mater.*, 2021, **9**, 2001572.
19 M. Alaasar, A. F. Darweesh, X. Cai, Y. Cao, F. Liu and C. Tschierske, *Chem. – Eur. J.*, 2021, **27**, 14921–14930.
20 M. Alaasar, S. Poppe, Q. Dong, F. Liu and C. Tschierske, *Chem. Commun.*, 2016, **52**, 13869–13872.
21 M. Alaasar, S. Poppe, Q. Dong, F. Liu and C. Tschierske, *Angew. Chem., Int. Ed.*, 2017, **56**, 10801–10805.
22 M. Alaasar, S. Poppe, Y. Cao, C. Chen, F. Liu, C. Zhu and C. Tschierske, *J. Mater. Chem. C*, 2020, **8**, 12902–12916.
23 M. Alaasar, M. Prehm, Y. Cao, F. Liu and C. Tschierske, *Angew. Chem., Int. Ed.*, 2016, **128**, 320–324.
24 M. Alaasar, J. C. Schmidt, X. Cai, F. Liu and C. Tschierske, *J. Mol. Liq.*, 2021, **332**, 115870–115880.
25 M. Alaasar, Y. Cao, Y. Liu, F. Liu and C. Tschierske, *Chem. – Eur. J.*, 2022, **28**, e202201857.
26 Y. Cao, M. Alaasar, L. Zhang, C. Zhu, C. Tschierske and F. Liu, *J. Am. Chem. Soc.*, 2022, **144**, 6936–6945.
27 C. Tschierske and G. Ungar, *ChemPhysChem*, 2016, **17**, 1224–1251.
28 A. H. Schoen, *Interface Focus*, 2012, **2**, 658–668.
29 S. Kutsumizu, *Isr. J. Chem.*, 2012, **52**, 844–853.
30 L. Han and S. Che, *Adv. Mater.*, 2018, **30**, 1705708.
31 M. L. Lynch and P. T. Spicer, *Bicontinuous Liquid Crystals*, CRC Press, Taylor & Francis Group, Boca Raton, FL, 2005.
32 X. Zeng and G. Ungar, *J. Mater. Chem. C*, 2020, **8**, 5389–5398.
33 C. Dressel, F. Liu, M. Prehm, X. B. Zeng, G. Ungar and C. Tschierske, *Angew. Chem., Int. Ed.*, 2014, **53**, 13115–13120.
34 Y. Cao, M. Alaasar, A. Nallapaneni, M. Salamończyk, P. Marinko, E. Gorecka, C. Tschierske, F. Liu, N. Vaupotič and C. Zhu, *Phys. Rev. Lett.*, 2020, **125**, 027801.
35 E. Cruickshank, G. J. Strachan, J. M. Storey and C. T. Imrie, *J. Mol. Liq.*, 2022, **346**, 117094.
36 Y. Arakawa, Y. Ishida, Y. Sasaki, S. Sasaki, M. Tokita and H. Tsuji, *Mater. Adv.*, 2022, **3**, 3218–3228.
37 Y. Arakawa, S. Inui and H. Tsuji, *Liq. Cryst.*, 2018, **45**, 811–820.
38 Y. Arakawa, Y. Sasaki, K. Igawa and H. Tsuji, *New J. Chem.*, 2017, **41**, 6514–6522.
39 Y. Arakawa, Y. Sasaki and H. Tsuji, *Chem. Lett.*, 2017, **46**, 1657–1659.

40 M. Alaasar, C. Anders, R. Pashameah and A. F. Darweesh, *Liq. Cryst.*, DOI: 10.1080/02678292.2023.2253199.
41 Y. Arakawa and H. Tsuji, *Mol. Cryst. Liq. Cryst.*, 2017, **647**, 422–429.
42 Y. Arakawa, S. Kang, H. Tsuji, J. Watanabe and G. I. Konishi, *RSC Adv.*, 2016, **6**, 16568–16574.
43 Y. Arakawa, Y. Sasaki, N. Haraguchi, S. Itsuno and H. Tsuji, *Liq. Cryst.*, 2018, **45**, 821–830.
44 G. W. Gray and S. M. Kelly, *J. Mater. Chem.*, 1999, **9**, 2037–2050.
45 P. Kirsch and M. Bremer, *Angew. Chem., Int. Ed.*, 2000, **39**, 4216–4235.
46 H. R. Stapert, S. Del Valle, E. J. K. Verstegen, B. M. I. Van der Zande, J. Lub and S. Stallinga, *Adv. Funct. Mater.*, 2003, **13**, 732–738.
47 N. Bennis, T. Jankowski, O. Strzezysz, A. Pakua, D. C. Zografopoulos, P. Perkowski, J. M. Sánchez-Pena, J. M. López-Higuera and J. F. Algorri, *Sci. Rep.*, 2022, **12**, 1–12.
48 M. G. Chee, M. H. Song, D. Kim, H. Takezoe and I. J. Chung, *Jpn. J. Appl. Phys., Part 2*, 2007, **46**, L437.
49 A. J. Seed, K. J. Toyne, J. W. Goodby and D. G. McDonnell, *J. Mater. Chem.*, 1995, **5**, 1–11.
50 A. Kumar and V. Molinero, *J. Phys. Chem. B*, 2018, **122**, 4758.
51 T. Sakaizumi, M. Namikawa and O. Ohashi, *J. Mol. Struct.*, 1995, **345**, 189–195.
52 J. Hine, *Reaktivität und Mechanismus in der Organischen Chemie*, Thieme, Stuttgart, 1960.
53 F. G. Riddell, *The conformational analysis of Heterocyclic compounds*, Academic Press, 1980.
54 E. Kleinpeter, H. Köhler, A. Lunow, C. Tschierske and H. Zaschke, *Tetrahedron*, 1988, **44**, 1609–1612.
55 Y. Arakawa, Y. Ishida, T. Shiba, K. Igawa, S. Sasaki and H. Tsuji, *CrystEngComm*, 2022, **24**, 1877–1890.
56 K. Iakoubovskii and M. Yoshio, *Chem. Commun.*, 2023, **59**, 7443–7446.
57 B. Ouyang, Y. Wang, R. Zhang, H. Olin and Y. Yang, *Cell Rep. Phys. Sci.*, 2021, **2**, 100418.